Elastic actions exchanged by eccentric cylinders in liquid crystals

Riccardo Rosso,[1] Epifanio G. Virga,[1] and Samo Kralj[2,3]
[1]*Dipartimento di Matematica and CNISM, Università di Pavia, via Ferrata 1, I-27100 Pavia, Italy*
[2]*Laboratory of Physics of Complex Systems, Faculty of Natural Sciences and Mathematics, University of Maribor, Koroška 160, 2000 Maribor, Slovenia*
[3]*Condensed Matter Physics Department, Jožef Stefan Institute, Jamova 39, 1000 Ljubljana, Slovenia*
(Received 24 April 2006; revised manuscript received 2 October 2006; published 21 December 2006)

Equilibria of a nematic liquid crystal confined between two eccentric cylinders are studied within a purely director approach. A planar equilibrium configuration competes against a three-dimensional one. A stability diagram is obtained in terms of both the ratio between the radii of the bounding cylinders and the distance between their axes. It turns out that the nonplanar minimizer has a structure more complex than that envisaged in the tensorial approach employed by McKay and Virga [Phys. Rev. E **71**, 041702 (2005)] and that the planar configuration cannot be the absolute minimizer when the outer cylinder becomes a plane wall. The mechanical actions transmitted by the nematic liquid crystal on both bounding cylinders are computed and compared with other results available in the literature.

DOI: 10.1103/PhysRevE.74.061703 PACS number(s): 61.30.Dk, 64.70.Md

I. INTRODUCTION

In the past two decades, experimental techniques based on the surface force apparatus made it possible to measure forces between solid objects submerged in liquid crystals. In their seminal paper, Horn *et al.* [1] introduced the notion of *structural forces* exchanged by solid surfaces through an intervening liquid crystal. These forces reveal the order modulations occurring within a liquid crystal interposed between rigid bodies, especially in the vicinity of their boundaries, where the anchoring to a material substrate has the potential to affect the surface ordering of the liquid crystal molecules in direct contact with the foreign bodies.

Recently, structural forces have been viewed as special cases of *order forces* [2], which result from more general alterations of the molecular order, similar to those establishing biaxial states in a defect core [3]. These biaxial states also arise in the presence of boundary frustration, when antagonistic anchorings are enforced on surfaces brought near to one another. Upon reducing the distance between the bounding surfaces, order transitions can be induced in bulk by bridging antagonistic, uniaxial states through a continuum of biaxial states: one uniaxial order is thus destroyed, while the other is being reconstructed. This phenomenon is often referred to as *order reconstruction* [4–7]: it can be revealed by the order force exchanged by surfaces with antagonistic anchorings. Precisely, it has been shown that order reconstruction weakens the repulsion between antagonistic anchorings [8]. This force, which in the absence of order reconstruction would be repulsive at all separations between the frustrating surfaces, and increasingly so when the separation is steadily reduced, falls momentarily as a consequence of order reconstruction when the repelling surfaces are a few biaxial coherence lengths ξ_b's apart (with ξ_b in the range of nanometers). This lack of monotonicity would induce a *snapping* instability in a force-controlled experiment with an ideal machine that could explore distances comparable with ξ_b. A similar behavior is also exhibited by the torque transmitted from one anchoring surface to the other [2,8]; actually, the transition predicted in a torque-controlled experiment is neater, as the torque drops to zero at the transition and this happens for separations larger than those required by the force-driven transition.

These predictions were made for a twist cell and a first, though indirect, experimental confirmation was later found for the classical surface force apparatus [9]. A geometry similar to that of the actual experiment was considered in [10], where both force and torque transmitted between a circular cylinder and a flat wall were computed, under the assumption of homeotropic anchoring on both surfaces, i.e., with molecules parallel to the surface unit normal. Elementary symmetry considerations show that this problem is equivalent to that where two equal cylinders with parallel axes are drawn close together. This study revealed a lack of monotonicity in both the force and the torque diagrams—attributed to curvature frustration rather than to order reconstruction—and predicted a snapping transition similar to that found experimentally [9], but for larger distances.

A previous study [11] had already been concerned with this problem within the director theory of nematic liquid crystals: the transmitted force computed for the planar equilibrium solution—with the director everywhere in the plane orthogonal to the cylinder's axis—exhibited a monotonic behavior, diverging like $1/\sqrt{h}$ as the distance h between cylinder and wall decreases to zero. It was shown in [10] that whenever h is smaller than a few times the radius R of the cylinder the planar director solution is unstable against a class of biaxial perturbations that render $\boldsymbol{n}$ *escaped* [12] in the direction of the cylinder's axis, so that the asymptotic behavior of the transmitted force was computed in [11] for a solution that is unlikely attained in reality when cylinder and wall are very close to one another. Similarly, the study reported in [10] is not exempt from criticism: the escaped solution was computed within the order tensor theory and biaxial states were allowed alongside of the uniaxial ones, but for computational ease the eigenframe of the order tensor was constrained within a class of orientations, which, though supported by intuition, were yet restricted. We wonder

whether unleashing the tensor eigenframe would remove the frustration that might have driven the lack of monotonicity in both the force and torque diagrams of [10]. This state of affairs demands a deeper study of both elastic force and torque exchanged by cylinder and wall, to probe the outcomes of [10,11]. Such a study is the motivation for this paper, which treats the more general problem of computing the elastic actions exchanged by two eccentric cylinders enclosing a nematic liquid crystal with homeotropic anchoring on both surfaces. We adopt the director description of the nematic phase, but we do not restrain the class of its possible orientations. Seen in the perspective of the order-tensor description, this assumption amounts to freezing a uniaxial order, while leaving the tensor eigenframe completely free.

The paper is organized as follows. In Sec. II we illustrate the geometry of the problem, and we recall the basic properties of bipolar cylindric coordinates, widely used below. We identify a planar equilibrium profile for the director field $\boldsymbol{n}$, the local stability of which is studied in Sec. III by a general stability criterion [13]. The range of stability of this solution is described in terms of two independent geometric parameters. Outside this range, the stable equilibrium configuration of $\boldsymbol{n}$ is escaped along the axis of both cylinders; this configuration is found numerically in Sec. IV. The elastic actions transmitted to the inner cylinder by the escaped solution are computed numerically in Sec. V. In Sec. VI we summarize our conclusions and contrast them with those of the papers that motivated this study [10,11]. Three Appendixes complete the paper: the first collects the details on cylindric bipolar coordinates needed here; the second outlines the numerical methods adopted in this paper, and the third applies the stability criterion of [13] to derive the bifurcation threshold obtained differently in [14] for the special case of two coaxial cylinders.

II. ECCENTRIC CYLINDERS

In the one-constant approximation, where all bulk elastic constants have one and the same positive value κ, the elastic free energy stored within a region $\mathcal{B}$ filled with liquid crystal is given by

$$\mathcal{F}[\boldsymbol{n}] := \frac{\kappa}{2}\int_{\mathcal{B}} |\nabla \boldsymbol{n}|^2 dV, \tag{2.1}$$

where V is the volume measure and $\boldsymbol{n}$ is a unit vector field representing everywhere the nematic director. Here we take $\mathcal{B}$ as the region between two parallel cylinders of radii r_i and $r_o > r_i$, with axes d apart (Fig. 1). We assume that strong, homeotropic boundary conditions are imposed on both the inner and the outer cylinder. The equilibrium configurations of $\boldsymbol{n}$ solve the Euler equation associated with $\mathcal{F}$:

$$\kappa \Delta \boldsymbol{n} = -\lambda \boldsymbol{n}, \tag{2.2}$$

where Δ is the Laplace operator and λ is a multiplier accounting for the constraint on the modulus of $\boldsymbol{n}$. By taking the inner product of both sides of Eq. (2.2) with $\boldsymbol{n}$, since $(\nabla \boldsymbol{n})^{\mathrm{T}}\boldsymbol{n} = 0$, Eq. (2.2) can be recast as

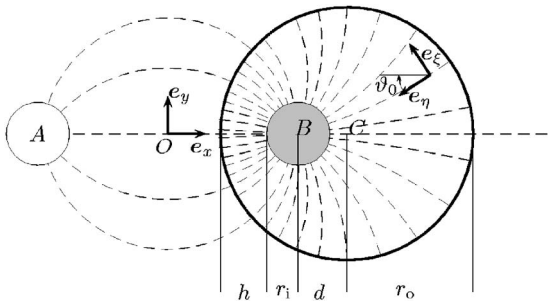

FIG. 1. Cross section of the region between two eccentric cylinders with radii r_i and $r_o > r_i$. The dashed curves are everywhere tangent to the field $\boldsymbol{e}_\eta$ and they are orthogonal to the lateral boundaries of both cylinders. These curves focus at the points $B \equiv (c,0)$ and $A \equiv (-c,0)$. O is the origin of the Cartesian coordinates and $C \equiv (c+d,0)$ lies on the axis of the outer cilynder. The distance between the inner and outer cylinders is $h = r_o - r_i - d$.

$$\Delta \boldsymbol{n} + |\nabla \boldsymbol{n}|^2 \boldsymbol{n} = \boldsymbol{0}, \tag{2.3}$$

which is clearly nonlinear.

As in [10,11], in solving Eq. (2.3) it is natural to use cylindric bipolar coordinates, which we now introduce following Appendix A of [15]. The Cartesian coordinates (x,y) of a point with bipolar coordinates (ξ,η) are (see Fig. 1)

$$x = c\frac{\sinh \eta}{\cosh \eta - \cos \xi}$$

$$y = c\frac{\sin \xi}{\cosh \eta - \cos \xi}, \tag{2.4}$$

where $c > 0$ is a parameter. The curves $\eta = \text{const}$ form a family of nonintersecting coaxial circles. Precisely, the circle $\eta = \eta_0$ has radius $c|\operatorname{cosech} \eta_0|$ and is centered at the point with Cartesian coordinates $(c \coth \eta_0, 0)$. Moreover, all the circles in this family surround the point $B \equiv (c,0)$. The curves $\xi = \xi_0 = \text{const}$ are circular arcs, centered along the y-axis at $(0, c \cot \xi_0)$, with radius $c|\operatorname{cosec} \xi_0|$. Precisely, for a given $\xi_0 \in (0,\pi)$, Eqs. (2.4) describe an arc with $y > 0$; for the same ξ_0 augmented by π, Eqs. (2.4) describe the arc with $y < 0$ on the same circle. All these arcs intersect at B and at $A \equiv (-c,0)$. The curves $\eta = \text{const}$ and $\xi = \text{const}$ are mutually orthogonal so that, if we take $\eta = \eta_o > 0$ and $\eta = \eta_i > 0$ to represent the outer and inner cylinders of the capillary, the tangent unit vector $\boldsymbol{e}_\eta$ to the circles $\xi = \text{const}$ satisfies the boundary conditions imposed on the director field $\boldsymbol{n}$. To reproduce the geometry of the problem, the parameters η_o, η_i, and c must obey

$$c \operatorname{cosech} \eta_o = r_o,$$

$$c \operatorname{cosech} \eta_i = r_i,$$

$$c[\coth \eta_o - \coth \eta_i] = d, \tag{2.5}$$

with $0 < \eta_o < \eta_i$. By setting

$$t_o := \sinh \eta_o, \quad t_i := \sinh \eta_i, \tag{2.6}$$

conditions (2.5) can be written in terms of the dimensionless parameters

$$\varrho := \frac{r_o}{r_i} > 1 \text{ and } \delta := \frac{d}{r_i} \in [0, \varrho - 1] \tag{2.7}$$

as

$$t_o r_o = t_i r_i \tag{2.8a}$$

$$\varrho\sqrt{1+t_o^2} - \sqrt{1+t_i^2} = \delta. \tag{2.8b}$$

Since, by Eq. (2.6), $t_i = t_o\varrho$, we can rewrite Eq. (2.8b) as

$$\varrho\sqrt{1+t_o^2} - \delta = \sqrt{1+(t_o\varrho)^2}, \tag{2.9}$$

whence, after some manipulations, we arrive at

$$\sinh \eta_o = \frac{1}{2\delta\varrho}\sqrt{[(\varrho-\delta)^2-1][(\varrho+\delta)^2-1]}. \tag{2.10}$$

Once Eq. (2.10) is inserted in Eq. (2.8a), this also yields η_i and c in terms of ϱ and δ, the only independent geometric parameters employed below:

$$\sinh \eta_i = \frac{1}{2\delta}\sqrt{[(\varrho-\delta)^2-1][(\varrho+\delta)^2-1]},$$

$$c = \frac{r_i}{2\delta}\sqrt{[(\varrho-\delta)^2-1][(\varrho+\delta)^2-1]}. \tag{2.11}$$

The distance h between the inner and the outer cylinders is given by

$$h = r_o - r_i - d$$

or, by rescaling all lengths to r_i, by

$$\chi := \frac{h}{r_i} = \varrho - 1 - \delta. \tag{2.12}$$

For given ϱ and δ as in Eq. (2.7), the eccentric annulus depicted in Fig. 1 is represented by the inequalities $0 \leqslant \xi \leqslant 2\pi$ and $\eta_o < \eta < \eta_i$.

The director field $\boldsymbol{n}_0 \equiv \boldsymbol{e}_\eta$ solves Eq. (2.2) for all admissible values of ϱ and δ, since it follows from Eqs. (A11) and (A12) of Appendix A that

$$\Delta \boldsymbol{e}_\eta = -\frac{1}{c^2}(\cosh^2 \eta - \cos^2 \xi)\boldsymbol{e}_\eta. \tag{2.13}$$

In the sequel, we often refer to $\boldsymbol{n}_0$ as the *planar* solution of this equilibrium problem. In the next section we study the local stability of $\boldsymbol{n}_0$, when ϱ and δ are varied.

III. STABILITY OF THE PLANAR SOLUTION

Here we apply to the planar solution $\boldsymbol{n}_0 \equiv \boldsymbol{e}_\eta$ the local stability criterion worked out in [13]. The equation obeyed by the field $\boldsymbol{u}$ perturbing $\boldsymbol{n}_0$ is central to the application of this criterion; it reads as

$$\Delta \boldsymbol{u} + \left(\mu + \frac{\lambda}{\kappa}\right)\boldsymbol{u} = \nu \boldsymbol{n}_0, \tag{3.1}$$

where

$$\frac{\lambda}{\kappa} = \frac{1}{c^2}(\cosh^2 \eta - \cos^2 \xi)$$

and ν and μ are Lagrange multipliers associated with the constraints

$$\boldsymbol{u} \cdot \boldsymbol{n}_0 = 0 \tag{3.2}$$

and

$$\int_{\mathcal{B}} \boldsymbol{u}^2 dV = 1, \tag{3.3}$$

respectively. The minimum value $\mu_{\min}$ of μ for which there are solutions to Eq. (3.1) subject to Eqs. (3.2) and (3.3) is also the minimum attained by the second variation of the energy functional $\mathcal{F}$ at $\boldsymbol{n}_0$ upon the set of functions defined by Eq. (3.3) [13]. If $\mu_{\min}$ is positive then $\boldsymbol{n}_0$ is locally stable, if $\mu_{\min}$ is negative then $\boldsymbol{n}_0$ is locally unstable. For a given μ, the solutions to Eq. (3.1) represent director perturbing modes with a prescribed energy variation. The existence of modes with negative μ reveals an instability in the unperturbed field.

Since $\boldsymbol{n}_0 \equiv \boldsymbol{e}_\eta$, the constraint (3.2) is uniformly accounted for by taking

$$\boldsymbol{u} = u_\xi \boldsymbol{e}_\xi + u_z \boldsymbol{e}_z,$$

and then by setting $\nu = 0$ in Eq. (3.1). We further take $\mathcal{B}$ to be infinite along $\boldsymbol{e}_z$ and consider modes independent of z so that both u_ξ and u_z are functions of (ξ, η). Thus by Eq. (A13) of Appendix A,

$$\Delta \boldsymbol{u} = \left[\Delta u_\xi - \frac{u_\xi}{H}\Delta H\right]\boldsymbol{e}_\xi + \frac{2}{H}[(\boldsymbol{\nabla} u_\xi \times \boldsymbol{\nabla} H)\cdot \boldsymbol{e}_z]\boldsymbol{e}_\eta + \Delta u_z \boldsymbol{e}_z,$$

where

$$H := \frac{1}{c}(\cosh \eta - \cos \xi), \tag{3.4}$$

and the planar gradient $\boldsymbol{\nabla}_\parallel u_\xi$ defined in Eq. (A9) has been replaced by $\boldsymbol{\nabla} u_\xi$ since u_ξ is independent of z. The components of Eq. (3.1) in the movable frame $(\boldsymbol{e}_\xi, \boldsymbol{e}_\eta, \boldsymbol{e}_z)$ are then

$$\Delta u_\xi + \mu u_\xi = 0, \tag{3.5a}$$

$$(\boldsymbol{\nabla} u_\xi \times \boldsymbol{\nabla} H)\cdot \boldsymbol{e}_z = 0, \tag{3.5b}$$

$$\Delta u_z + \left[\mu + \frac{1}{c^2}(\cosh^2 \eta - \cos^2 \xi)\right]u_z = 0. \tag{3.5c}$$

In addition to Eq. (3.3), where the integral is now reduced over the cross section $\mathbb{B}$ of $\mathcal{B}$, these equations are also subject to the boundary conditions

$$u_\xi|_{\partial\mathbb{B}} = u_z|_{\partial\mathbb{B}} = 0, \tag{3.6}$$

since all modes must preserve the anchoring of $\boldsymbol{n}_0$.

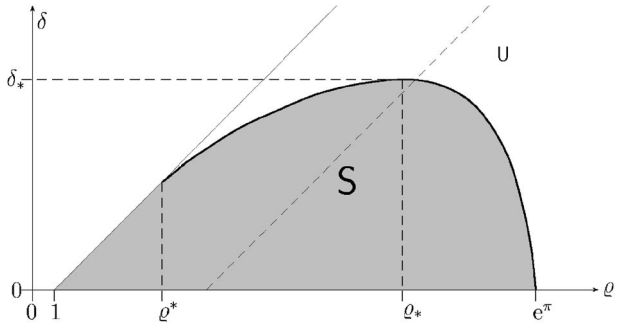

FIG. 2. Stability diagram in the (ϱ,δ) plane. The equilibrium configuration $\boldsymbol{n}_0 \equiv \boldsymbol{e}_\eta$ is locally stable in the region S, while it is unstable in the region U. The straight line $\delta=\varrho-1$ is the locus where the inner and outer cylinders are tangent to one another: only the region $\delta \leqslant \varrho-1$ in the positive quadrant of the (ϱ,δ) plane is admissible. In general, the dashed line $\delta=\varrho-1-\chi$ is the locus where the two cylinders are at a fixed scaled distance $\chi=h/r_\mathrm{i}$. Increasing ϱ along one of these lines amounts to increasing both the radius r_o of the outer cylinder and the eccentricity d, while keeping the distance between the cylinders fixed. Asymptotically, the outer cylinder becomes infinite. In that limit, the planar configuration $\boldsymbol{n}_0 \equiv \boldsymbol{e}_\eta$ is unstable, whatever be the distance between the cylinders. The path separating S and U touches the line $\delta=\varrho-1$ at $\varrho^* \approx 8.46$ and the line $\delta=0$ at $\varrho=e^\pi \approx 23.14$; the maximum extension in the δ-direction occurs at $\delta=\delta_* \approx 9.62$ and $\varrho=\varrho_* \approx 17.01$.

The analysis of Eqs. (3.5) can be simplified a great deal by showing that the component u_ξ alone cannot induce destabilizing modes. Suppose for a contradiction that a nonzero solution of Eq. (3.5a) exists. By multiplying both sides of Eq. (3.5a) by u_ξ and then integrating in $\mathbb{B}$ we readily arrive at

$$\int_{\mathbb{B}} [\mathrm{div}(u_\xi \nabla u_\xi) - (\nabla u_\xi)^2 + \mu u_\xi^2] dA = 0,$$

where A is the area measure. Finally, use of the divergence theorem and of the boundary conditions (3.6) yields

$$\int_{\mathbb{B}} [\mu u_\xi^2 - (\nabla u_\xi)^2] dV = 0,$$

whence it follows that $\mu > 0$. Since a destabilizing mode exists only if $\mu \leqslant 0$, it requires that $u_\xi \equiv 0$, and so Eq. (3.5b) is identically satisfied.

Setting $\mu=0$ in Eq. (3.5c) detects the onset of instability: the corresponding *marginal* modes, if existing, represent distortions of the planar solution $\boldsymbol{n}_0$ that bear no extra elastic energy up to the second order in the perturbation norm. For $\mu=0$, Eq. (3.5c) becomes

$$\frac{\partial^2 u_z}{\partial \xi^2} + \frac{\partial^2 u_z}{\partial \eta^2} + \frac{\cosh\eta + \cos\xi}{\cosh\eta - \cos\xi} u_z = 0, \tag{3.7}$$

subject to the following boundary conditions in η:

$$u_z(\xi,\eta_\mathrm{o}) = u_z(\xi,\eta_\mathrm{i}) = 0, \quad \forall\, \xi \in [0,2\pi] \tag{3.8}$$

and to periodic boundary conditions in ξ. Equations (3.7) and (3.8) were solved numerically (see Appendix B for details). Figure 2 shows the path on the (ϱ,δ) plane along which we found a nonzero solution to these equations. By Eq. (2.7), only the set $\delta \leqslant \varrho-1$ is admissible in the (ϱ,δ) plane. The path shown in Fig. 2 intersects the line $\delta=\varrho-1$ at $\varrho=\varrho^* \approx 8.46$ and the line $\delta=0$ at $\varrho=e^\pi \approx 23.14$. The case $\delta=0$, where the two cylinders are coaxial, has already been treated in [14]: there the stability analysis was brought far beyond the marginal modes, and the planar, radial solution $\boldsymbol{n}_0$ was shown to be locally stable for $\varrho < \mathrm{e}^\pi$ and locally unstable for $\varrho > \mathrm{e}^\pi$. Our method is capable of arriving differently at the same conclusion (see Appendix C). Here we heed that this result has consequences on the problem at hand: by continuity, we conclude that for $\delta > 0$ the region S delimited in Fig. 2 by the path of marginal modes is the stability domain for the planar solution $\boldsymbol{n}_0 \equiv \boldsymbol{e}_\eta$. Correspondingly, the complementary region U is the domain of instability.

According to Eq. (2.12), all straight lines in the (ϱ,δ) plane parallel to $\delta=\varrho-1$ represent cylinders with different radii r_i and r_o, but equal normalized separation $\chi=h/r_\mathrm{i}$. One such line is represented in Fig. 2 as a dashed line: in the limit as $\varrho \to \infty$, the outer cylinder approaches a flat wall at the prescribed distance from the inner cylinder. Whatever the value of χ, the planar solution $\boldsymbol{n}_0$ becomes unstable for sufficiently large values of ϱ. For given ϱ, increasing δ towards its allowed maximum $\varrho-1$ reduces down to nothing the separation between cylinders of fixed radii. If $\varrho < \varrho^*$, the planar solution remains stable for all separations between the cylinders. If $\varrho > \varrho^*$, the planar solution becomes eventually unstable before the cylinders are brought in contact. In particular, the planar solution between a cylinder and a flat wall with homeotropic anchoring is unstable, whatever be the separation between cylinder and wall.

Whenever the planar solution $\boldsymbol{n}_0 \equiv \boldsymbol{e}_\eta$ is unstable, the elastic free energy $\mathcal{F}$ is bound to decrease if the director $\boldsymbol{n}$ flips out the $(\boldsymbol{e}_\xi, \boldsymbol{e}_\eta)$ plane, thus acquiring a component along $\boldsymbol{e}_z$. The nature of this *escaped* solution that replaces $\boldsymbol{n}_0$ as energy minimizer is explored in the following section. In our numerical exploration, the transition to the escaped solution prompted by the instability of the planar solution was found to be continuous, with no hysteresis, and so, in the language of critical phenomena, we may say that this is a second-order transition.

IV. ESCAPED SOLUTION

Here, we study in detail the structure of the locally stable equilibrium configuration that bifurcates from $\boldsymbol{n}_0 \equiv \boldsymbol{e}_\eta$ when the parameters are chosen in the region U of the (ϱ,δ) plane. We shall solve numerically the equilibrium equation by the over-relaxation method [16] (see Appendix B for details). First, we parametrize the director field $\boldsymbol{n}$ as

$$\boldsymbol{n} = \sin\vartheta \cos\varphi \boldsymbol{e}_\xi + \cos\vartheta \cos\varphi \boldsymbol{e}_\eta + \sin\varphi \boldsymbol{e}_z, \tag{4.1}$$

where the angle $\varphi \in [-\pi/2, \pi/2]$ measures the escape of $\boldsymbol{n}$ out of the $(\boldsymbol{e}_\xi, \boldsymbol{e}_\eta)$ plane, and $\vartheta \in [-\pi/2, \pi/2]$ measures how much the planar projection of $\boldsymbol{n}$ wobbles about $\boldsymbol{e}_\eta$. The restrictions imposed on ϑ and φ reduce Eq. (4.1) to describe half a sphere around the axis $\boldsymbol{e}_\eta$, thus removing the usual degeneracy that regards $\boldsymbol{n}$ and $-\boldsymbol{n}$ as equivalent. We seek

solutions to Eq. (2.3) in the form (4.1), where both ϑ and φ depend on ξ and η, but are independent of z. By Eq. (A10), perusal of Eqs. (A3)–(A9) combined with algebraic manipulations yield

$$|\nabla \boldsymbol{n}|^2 = H^2\left\{\varphi_{,\xi}^2+\varphi_{,\eta}^2+\cos^2\varphi\left[\left(\vartheta_{,\xi}-\frac{\sinh\eta}{\cosh\eta-\cos\xi}\right)^2+\left(\vartheta_{,\eta}+\frac{\sin\xi}{\cosh\eta-\cos\xi}\right)^2\right]\right\}, \tag{4.2}$$

where a comma stands for partial differentiation. Since the Jacobian of the change of variables (2.4) is $|J|=1/H^2$, it follows from Eq. (2.1) that the elastic energy $\mathbb{F}$ per unit height of the cylinder is

$$\mathbb{F}[\boldsymbol{n}] := \frac{\kappa}{2}\int_{\eta_o}^{\eta_i} d\eta \int_0^{2\pi} d\xi\sigma, \tag{4.3}$$

where, with the aid of Eq. (4.2), σ is defined by setting $H^2\sigma := |\nabla \boldsymbol{n}|^2$. The Euler equations associated with Eq. (4.3) are

$$\frac{\partial}{\partial\xi}\left(\frac{\partial\sigma}{\partial\vartheta_{,\xi}}\right)+\frac{\partial}{\partial\eta}\left(\frac{\partial\sigma}{\partial\vartheta_{,\eta}}\right)-\frac{\partial\sigma}{\partial\vartheta}=0, \tag{4.4a}$$

$$\frac{\partial}{\partial\xi}\left(\frac{\partial\sigma}{\partial\varphi_{,\xi}}\right)+\frac{\partial}{\partial\eta}\left(\frac{\partial\sigma}{\partial\varphi_{,\eta}}\right)-\frac{\partial\sigma}{\partial\varphi}=0, \tag{4.4b}$$

which, by Eq. (4.2), explicitly read as

$$\cos^2\varphi(\vartheta_{,\xi\xi}+\vartheta_{,\eta\eta})-2\sin\varphi\cos\varphi\left(\vartheta_{,\xi}\varphi_{,\xi}+\vartheta_{,\eta}\varphi_{,\eta}+\frac{1}{\cosh\eta-\cos\xi}(\sin\xi\varphi_{,\eta}-\sinh\eta\varphi_{,\xi})\right)=0, \tag{4.5a}$$

$$\varphi_{,\xi\xi}+\varphi_{,\eta\eta}+\sin\varphi\cos\varphi\left[\left(\vartheta_{,\xi}-\frac{\sinh\eta}{\cosh\eta-\cos\xi}\right)^2+\left(\vartheta_{,\eta}+\frac{\sin\xi}{\cosh\eta-\cos\xi}\right)^2\right]=0. \tag{4.5b}$$

Subjecting $\boldsymbol{n}$ in Eq. (4.1) to homeotropic boundary conditions on both cylinders at $\eta=\eta_o$ and $\eta=\eta_i$ amounts to requiring that

$$\vartheta(\xi,\eta_o)=\vartheta(\xi,\eta_i)=0 \quad \text{and} \quad \varphi(\xi,\eta_o)=\varphi(\xi,\eta_i)=0, \quad \forall\,\xi\in[0,2\pi] \tag{4.6}$$

and to subjecting both ϑ and φ to periodic boundary conditions at $\xi=0$ and $\xi=2\pi$. It follows from Eqs. (4.5a) and $(4.6)_1$ that there are no equilibrium director fields in the $(\boldsymbol{e}_\eta,\boldsymbol{e}_z)$ plane, apart from $\boldsymbol{n}\equiv\boldsymbol{e}_\eta$. To see this, we set $\vartheta\equiv 0$ in Eq. (4.5a), which by Eq. $(4.6)_2$ is thus resolved in a dichotomy: either $\varphi\equiv 0$ or

$$\sin\xi\varphi_{,\eta}-\sinh\eta\varphi_{,\xi}\equiv 0. \tag{4.7}$$

Now, since $H>0$, it follows from Eqs. (3.4) and (A7) that Eq. (4.7) is equivalent to

$$\nabla H\times\nabla\varphi=\frac{H^2}{c}(\sin\xi\varphi_{,\eta}-\sinh\eta\varphi_{,\xi})\boldsymbol{e}_z=\boldsymbol{0}.$$

Thus if $\nabla\varphi$ does not vanish identically, it must be parallel to ∇H. In particular, this implies that $\nabla H\cdot\boldsymbol{e}_\xi=0$ at both $\eta=\eta_i$ and $\eta=\eta_o$. Since $\nabla H\cdot\boldsymbol{e}_\xi=H/c\,\sin\xi$ does not vanish identically for any given η, we conclude that $\vartheta\equiv 0\Rightarrow\varphi\equiv 0$.

There is an even more concise way to express σ in Eq. (4.3). By Eq. (A4), the angle ϑ_0 that $\boldsymbol{e}_\eta$ makes with $-\boldsymbol{e}_x$ (see also Fig. 1) is characterized by

$$\cos\vartheta_0=\frac{\cosh\eta\cos\xi-1}{\cosh\eta-\cos\xi}. \tag{4.8}$$

For given η, ϑ_0 ranges in the interval $[0,\pi]$ for $\xi\in[0,\pi]$, and in the interval $[-\pi,0]$ for $\xi\in[\pi,2\pi]$. Inverting separately in these intervals the function ϑ_0 defined by Eq. (4.8), one shows that

$$\vartheta_{0,\xi}=\frac{\sinh\eta}{\cosh\eta-\cos\xi} \text{ and } \vartheta_{0,\eta}=-\frac{\sin\xi}{\cosh\eta-\cos\xi}. \tag{4.9}$$

Thus letting $\psi := \vartheta-\vartheta_0$ denote the angle that the projection of $\boldsymbol{n}$ on the plane $(\boldsymbol{e}_x,\boldsymbol{e}_y)$ makes with $-\boldsymbol{e}_x$ (see Fig. 1), we can rewrite σ as

$$\sigma=(\varphi_{,\xi}^2+\varphi_{,\eta}^2)+\cos^2\varphi(\psi_{,\xi}^2+\psi_{,\eta}^2). \tag{4.10}$$

It follows from Eqs. (4.6) and (4.8) that $\psi=-\vartheta_0$ for both $\eta=\eta_o,\eta_i$ and that ϑ_0 is odd relative to the mirror symmetry about the line $\xi=\pi$: formally, $\vartheta_0(2\pi-\xi,\eta)=-\vartheta_0(\xi,\eta)$. Moreover, ψ is subject like ϑ to periodic boundary conditions at $\xi=0$ and $\xi=2\pi$. Equation (4.10) illustrates well the competition between planar and escaped director configurations: while a planar field with $\varphi\equiv 0$ would minimize the first bracket, it cannot make the second identically zero as well since this would reduce $\boldsymbol{n}$ to $\boldsymbol{e}_x$ thus violating the anchoring conditions on the bounding cylinders. Hence $(\psi_{,\xi}^2+\psi_{,\eta}^2)$ can be viewed as the cost that a planar configuration has to pay to obey the boundary conditions. This frustration involves larger distortions of ψ, which can be partly relaxed if the $\cos^2\varphi$ factor in Eq. (4.10) becomes strictly less than 1, that is, if the director field flips out of the $(\boldsymbol{e}_x,\boldsymbol{e}_y)$ plane. Such a gain in energy will have to be balanced against the cost incurred in the bracket $(\varphi_{,\xi}^2+\varphi_{,\eta}^2)$. That cost will be higher in the gap between the inner cylinder and the outer cylinder, which is why one expects to see the out-of-plane structure developing on the more spacious opposite side of the inner cylinder.

Among the solutions to Eqs. (4.5) the minimizers of $\mathbb{F}$ were found by applying the relaxation method to appropriate initial guesses (see Appendix B). The scaled energy density σ in Eq. (4.10) is invariant under a change of sign in φ; this mirrors the symmetry between two opposite ways of escape for $\boldsymbol{n}$, that is, along $\boldsymbol{e}_z$ and along $-\boldsymbol{e}_z$. To remove this obvious degeneracy, we restrain φ to the interval $[0,\pi/2]$. Within numerical accuracy, the minimizers of $\mathbb{F}$ thus found turned to enjoy the symmetry properties

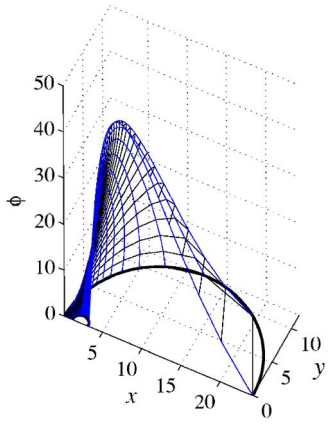

FIG. 3. (Color online) The 3D plot of $\varphi(x,y)$ when $\delta=10$ and $\varrho=12$. Since the solution is symmetric with respect to the $\boldsymbol{e}_x$ axis, only the half with $y\geqslant 0$ is drawn.

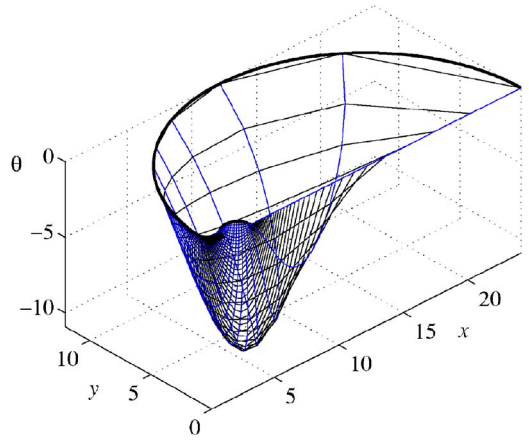

FIG. 4. (Color online) The 3D plot of $\vartheta(x,y)$ when $\delta=10$ and $\varrho=12$. As in Fig. 3, only the half with $y\geqslant 0$ is drawn.

$$\vartheta(2\pi-\xi,\eta)=-\vartheta(\xi,\eta),\quad \varphi(2\pi-\xi,\eta)=\varphi(\xi,\eta),\quad \forall\ \eta\in[\eta_o,\eta_i]. \tag{4.11}$$

Differently said, ϑ and φ are found odd and even, respectively, relative to the mirror symmetry about $\xi=\pi$. Likewise, by Eq. (4.8), ψ is also odd. Since, by Eq. (2.4), both $\xi=0$ and $\xi=\pi$ correspond to $y=0$, by use of Eqs. (4.1), (A3), and (A4), Eqs. (4.4) make the corresponding director field $\boldsymbol{n}$ in space mirror symmetric relative to the $(\boldsymbol{e}_x,\boldsymbol{e}_z)$ plane. It is readily shown that both the energy density (4.10) and the equilibrium equations (4.5) are invariant under the transformation in Eq. (4.11). Though this does not suffice to prove that all energy minimizers are mirror symmetric with respect to the plane $(\boldsymbol{e}_x,\boldsymbol{e}_z)$, it supports the numerical evidence. Analytically, Steiner's symmetry rearrangement applied to a tentative minimizer φ fails to imply by classical theorems that the actual minimizer φ is symmetric about $\xi=\pi$, as the function $(\psi_{,\xi}^2+\psi_{,\eta}^2)$ in Eq. (4.10) cannot be assumed to depend on η only (see Theorem 2.31 of [17]).

In the following we shall assume that Eqs. (4.11) hold and we shall represent both φ and ϑ only for $\xi\in[0,\pi]$, though they are obtained by the relaxation method in the whole interval $[0,2\pi]$.

Figures 3 and 4 show the three-dimensional (3D) plots of $\varphi(x,y)$ and $\vartheta(x,y)$ for $y\geqslant 0$ when $\varrho=12$ and $\delta=10$: the former exhibits a bump, and the latter a dip. To study in more detail the structure of the escaped field, we determine the point $(\hat{\xi}_\varphi,\hat{\eta}_\varphi)$ where $\varphi(\xi,\eta)$ attains its maximum and the point $(\hat{\xi}_\vartheta,\hat{\eta}_\vartheta)$ where ϑ attains its minimum. In Fig. 5(a) are plotted the functions $\varphi(\xi,\hat{\eta}_\varphi)$ and $\vartheta(\xi,\hat{\eta}_\vartheta)$ against ξ, in Fig. 5(b) are plotted the functions $\varphi(\hat{\xi}_\varphi,\eta)$ and $\vartheta(\hat{\xi}_\vartheta,\eta)$ against η: they represent special curvilinear cross sections of the 3D plots shown in Figs. 3 and 4. Other cross sections look alike, apart from showing less pronounced bumps and dips. The escape of the equilibrium solution along $\boldsymbol{e}_z$ is larger than the wobbling of its projection onto the $(\boldsymbol{e}_\xi,\boldsymbol{e}_\eta)$ plane about $\boldsymbol{e}_\eta$. Figure 6 is the analog of Fig. 5 for $\delta=2$ and $\varrho=24$. In this case both ϑ and φ depend only weakly on ξ. This is indeed a general feature: when the eccentricity of the two cylinders

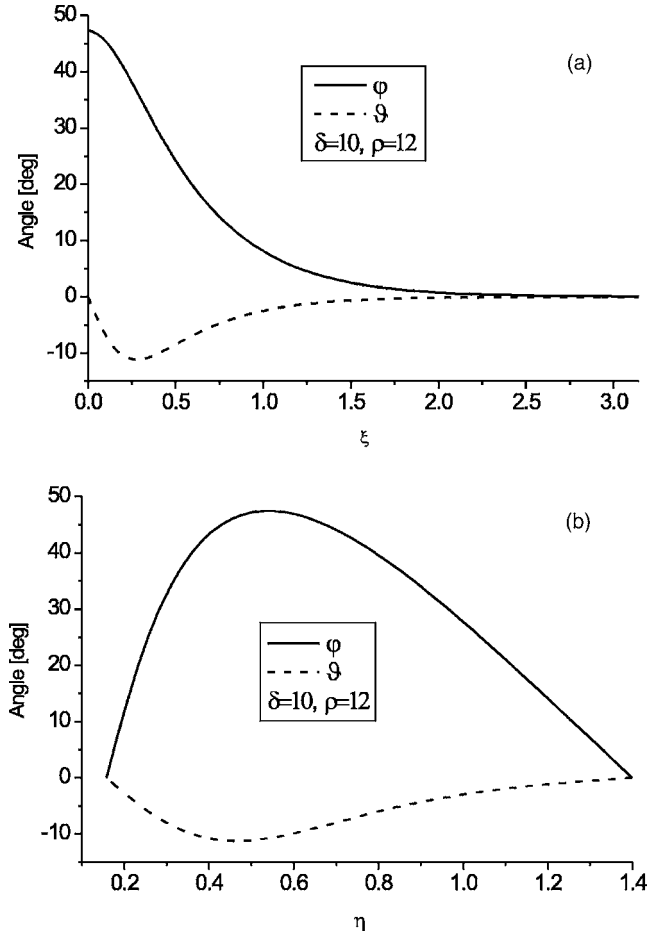

FIG. 5. Structural details of the escaped solution for $\delta=10$, $\varrho=12$. These plots are obtained by taking curvilinear cross sections of both 3D plots shown in Figs. 3 and 4. The cross sections of the graph of φ are at $\xi=\hat{\xi}_\varphi$ and $\eta=\hat{\eta}_\varphi$. The cross sections of the graph of ϑ are at $\xi=\hat{\xi}_\vartheta$ and $\eta=\hat{\eta}_\vartheta$. In (a) are plotted the functions $\varphi(\xi,\hat{\eta}_\varphi)$ (continuous line) and $\vartheta(\xi,\hat{\eta}_\vartheta)$ (dashed line) against $\xi\in[0,\pi]$. In (b) are plotted the functions $\varphi(\hat{\xi}_\varphi,\eta)$ (continuous line) and $\vartheta(\hat{\xi}_\vartheta,\eta)$ (dashed line) against $\eta\in[\eta_o,\eta_i]$.

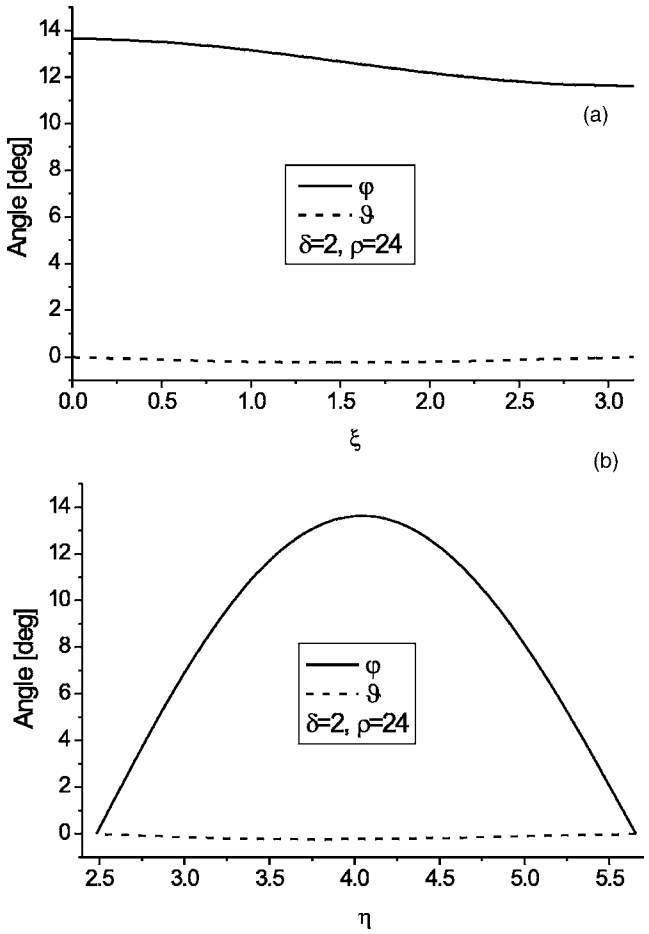

FIG. 6. Structural details of the escaped solution for $\delta=2$, $\varrho=24$. These plots were obtained precisely as in Fig. 5. Since here the eccentricity of the two cylinders is appreciably smaller than in Fig. 5 (δ is 2 instead of 10), both φ and ϑ depend weakly on ξ and ϑ scarcely departs from zero.

is small, the equilibrium director field resembles the one for $\delta=0$, which depends only on the radial coordinate r and lies in the $(\boldsymbol{e}_r,\boldsymbol{e}_z)$ plane [14] (see also Appendix C).

V. TRANSMITTED FORCE AND TORQUE

In this section we compute the force $\boldsymbol{F}$ and the torque $\boldsymbol{M}$ exerted on the inner cylinder when the nematic liquid crystal enclosed within the outer cylinder is in its locally stable equilibrium. By Newton's third law, the opposite force and torque are exerted on the outer cylinder. Before actually computing $\boldsymbol{F}$ and $\boldsymbol{M}$ we present a general symmetry argument that, once applied to the problem at hand, identifies the nontrivial components of both $\boldsymbol{F}$ and $\boldsymbol{M}$.

A. Symmetry

In general, a nematic liquid crystal transmits both a force $\boldsymbol{F}_{\mathcal{S}}$ and a couple $\boldsymbol{m}_{\mathcal{S}}$ onto an orientable surface $\mathcal{S}$ in contact with it: these mechanical actions are expressed by the formulas

$$\boldsymbol{F}_{\mathcal{S}}=\int_{\mathcal{S}}\mathbf{T}^{(E)}\boldsymbol{\nu}dA \tag{5.1}$$

and

$$\boldsymbol{m}_{\mathcal{S}}=\int_{\mathcal{S}}\mathbf{L}\boldsymbol{\nu}dA, \tag{5.2}$$

where $\boldsymbol{\nu}$ is the unit normal of $\mathcal{S}$ oriented towards the region occupied by the liquid crystal. In Eq. (5.1), $\mathbf{T}^{(E)}$ is Ericksen's stress tensor [18], which for a general elastic energy density $W=W(\boldsymbol{n},\boldsymbol{\nabla n})$ is given by

$$\mathbf{T}^{(E)}\boldsymbol{\nu}=W\boldsymbol{\nu}-(\boldsymbol{\nabla n})^{\mathrm{T}}\left(\frac{\partial W}{\partial\boldsymbol{\nabla n}}\right)\boldsymbol{\nu}, \tag{5.3}$$

for all unit vectors $\boldsymbol{\nu}$. In Eq. (5.2), $\mathbf{L}$ is Leslie's couple stress [19], which is defined by

$$\mathbf{L}\boldsymbol{\nu}=\boldsymbol{n}\times\left(\frac{\partial W}{\partial\boldsymbol{\nabla n}}\right)\boldsymbol{\nu}, \tag{5.4}$$

for all unit vectors $\boldsymbol{\nu}$. It follows from Eqs. (5.1) and (5.2) that the total torque $\boldsymbol{M}_{\mathcal{S}}$ exerted on $\mathcal{S}$ relative to a point o in space is given by

$$\boldsymbol{M}_{\mathcal{S}}=\int_{\mathcal{S}}\boldsymbol{x}\times\mathbf{T}^{(E)}\boldsymbol{\nu}dA+\boldsymbol{m}_{\mathcal{S}}, \tag{5.5}$$

where $\boldsymbol{x}:=p-o$ is the position vector of the current point p on $\mathcal{S}$.

Suppose now that the region $\mathcal{B}$ containing the liquid crystal and the director field $\boldsymbol{n}$ defined in $\mathcal{B}$ are subject to a transformation that maps a point $p\in\mathcal{B}$ into $p^*\in\mathcal{B}^*$ and assigns to p^* the director $\boldsymbol{n}^*(p^*)$ according to the stipulations

$$p^*-o=\mathbf{Q}(p-o), \tag{5.6}$$

$$\boldsymbol{n}^*(p^*)=\mathbf{Q}\boldsymbol{n}(p), \tag{5.7}$$

where $\mathbf{Q}$ is an orthogonal tensor, independent of the position p, for which

$$\mathbf{Q}^{\mathrm{T}}\mathbf{Q}=\mathbf{I}, \tag{5.8}$$

so that

$$\det\mathbf{Q}=\pm1. \tag{5.9}$$

Under the transformation in Eqs. (5.6) and (5.7), the tensors $\boldsymbol{\nabla n}$ and $\frac{\partial W}{\partial\boldsymbol{\nabla n}}$ are changed into

$$\boldsymbol{\nabla n}^*=\mathbf{Q}(\boldsymbol{\nabla n})\mathbf{Q}^{\mathrm{T}}\ \text{and}\ \frac{\partial W}{\partial\boldsymbol{\nabla n}^*}=\mathbf{Q}\left(\frac{\partial W}{\partial\boldsymbol{\nabla n}}\right)\mathbf{Q}^{\mathrm{T}}, \tag{5.10}$$

respectively, while W, being a scalar, is left unchanged (see Sec. 3.1.1 of [20]). Since the unit normal $\boldsymbol{\nu}$ to the point p^* on $\mathcal{S}^*$ is given by

$$\boldsymbol{\nu}^*=\mathbf{Q}\boldsymbol{\nu}, \tag{5.11}$$

we easily conclude from Eqs. (5.3), (5.8), and (5.10) that

$$\mathbf{T}^{(E)*}\boldsymbol{\nu}^* = \mathbf{Q}\mathbf{T}^{(E)}\boldsymbol{\nu}. \tag{5.12}$$

Similarly, by Eq. (5.4) and the property of the adjugate of a tensor (see Secs. 2.2.5 and 2.2.6 of [20]),

$$\mathbf{L}^*\boldsymbol{\nu}^* = \mathbf{Q}\boldsymbol{n} \times \mathbf{Q}\left(\frac{\partial W}{\partial \nabla \boldsymbol{n}}\right)\boldsymbol{\nu} = (\det \mathbf{Q})\mathbf{Q}\mathbf{L}\boldsymbol{\nu}. \tag{5.13}$$

By applying Eqs. (5.1) and (5.2) to the surface $\mathcal{S}^*$ and heeding that the Jacobian of the transformation (5.6) is 1, we conclude that the force $\boldsymbol{F}_{\mathcal{S}^*}$ and the couple $\boldsymbol{m}_{\mathcal{S}^*}$ acting on $\mathcal{S}^*$ are

$$\mathbf{F}_{\mathcal{S}^*} = \mathbf{Q}\mathbf{F}_{\mathcal{S}} \text{ and } \boldsymbol{m}_{\mathcal{S}^*} = (\det \mathbf{Q})\mathbf{Q}\boldsymbol{m}_{\mathcal{S}}. \tag{5.14}$$

Similarly, it follows from Eq. (5.5) that the total torque $\boldsymbol{M}_{\mathcal{S}^*}$ on $\mathcal{S}^*$ is

$$\mathbf{M}_{\mathcal{S}^*} = (\det \mathbf{Q})\mathbf{Q}\mathbf{M}_{\mathcal{S}}. \tag{5.15}$$

These equations relate in general the mechanical actions on $\mathcal{S}_*$ to those on $\mathcal{S}$. They become more stringent and predictive whenever Eqs. (5.6) and (5.7) describe a symmetry transformation for which $\mathcal{B}^*=\mathcal{B}$ and $\boldsymbol{n}^*=\boldsymbol{n}$. If this is the case, $\boldsymbol{F}_{\mathcal{S}^*}$, $\boldsymbol{m}_{\mathcal{S}^*}$, and $\boldsymbol{M}_{\mathcal{S}^*}$ are the same as $\boldsymbol{F}_{\mathcal{S}}$, $\boldsymbol{m}_{\mathcal{S}}$, and $\boldsymbol{M}_{\mathcal{S}}$, respectively, and so, by Eqs. (5.14), (5.15), and (5.9), $\boldsymbol{F}_{\mathcal{S}}$ is an eigenvector of $\mathbf{Q}$ with eigenvalue 1, while both $\boldsymbol{m}_{\mathcal{S}}$ and $\boldsymbol{M}_{\mathcal{S}}$ are eigenvectors of $\mathbf{Q}$ with eigenvalue $1/\det \mathbf{Q}$.

We now apply this theorem to the force $\boldsymbol{F}$ and the torque $\boldsymbol{M}$ exerted on the inner cylinder in our problem. The equilibrium director field $\boldsymbol{n}$ in the class we have chosen above is symmetric about the $(\boldsymbol{e}_x,\boldsymbol{e}_z)$ plane, that is, it obeys Eqs. (5.6) and (5.7) when $\mathbf{Q}$ is the reflection about this plane:

$$\mathbf{Q} = \mathbf{I} - 2\boldsymbol{e}_y \otimes \boldsymbol{e}_y, \tag{5.16}$$

for which $\det \mathbf{Q}=-1$. The only eigenvector of $\mathbf{Q}$ in Eq. (5.16) with eigenvalue -1 is $\boldsymbol{e}_y$, whereas both $\boldsymbol{e}_x$ and $\boldsymbol{e}_z$ are eigenvectors of $\mathbf{Q}$ with eigenvalue $+1$. Thus, by the theorem above,

$$\mathbf{F}\cdot\boldsymbol{e}_y = 0 \text{ and } \mathbf{M} = M\boldsymbol{e}_y. \tag{5.17}$$

In the problem at hand, the first of these equations can be further specialized. The admissible director fields $\boldsymbol{n}$ are taken here to be independent of z, and so $(\nabla\boldsymbol{n})\boldsymbol{e}_z=\mathbf{0}$. Moreover, for a cylinder parallel to the z axis the unit normal $\boldsymbol{\nu}$ to its lateral boundary is such that $\boldsymbol{\nu}\cdot\boldsymbol{e}_z\equiv 0$. Thus the surface traction in Eq. (5.3) satisfies

$$\boldsymbol{e}_z\cdot\mathbf{T}^{(E)}\boldsymbol{\nu} \equiv 0,$$

and so does $\boldsymbol{F}$. Hence

$$\mathbf{F} = F\boldsymbol{e}_x. \tag{5.18}$$

In the following two sections, we compute the nontrivial components of $\boldsymbol{F}$ and $\boldsymbol{M}$, that is, F and M in Eqs. (5.18) and (5.17).

B. Force

When $W=\frac{1}{2}\kappa|\nabla\boldsymbol{n}|^2$, as in Eq. (2.1), Ericksen's stress tensor reads

$$\mathbf{T}^{(E)} := \kappa\left[\frac{|\nabla\boldsymbol{n}|^2}{2}\mathbf{I} - (\nabla\boldsymbol{n})^{\mathrm{T}}(\nabla\boldsymbol{n})\right]. \tag{5.19}$$

Correspondingly, the nontrivial component of $\boldsymbol{F}$ per unit height of the inner cylinder is given by

$$F = \int_{\mathcal{C}} \boldsymbol{e}_x\cdot\mathbf{T}^{(E)}\boldsymbol{\nu}\,d\ell, \tag{5.20}$$

where $\mathcal{C}$ is the inner circle bounding $\mathbb{B}$, $\boldsymbol{\nu}=-\boldsymbol{e}_\eta$ is the outer unit normal vector to $\mathcal{C}$, and ℓ is the arclength along $\mathcal{C}$.

To give Eq. (5.20) a simple computable form, it is expedient to use the following hybrid representation for $\boldsymbol{n}$:

$$\boldsymbol{n} = \cos\varphi\cos\psi\boldsymbol{e}_x + \cos\varphi\sin\psi\boldsymbol{e}_y + \sin\varphi\boldsymbol{e}_z, \tag{5.21}$$

where, as above, $\psi=\vartheta-\vartheta_0$. It follows from Eq. (5.21) that

$$\nabla\boldsymbol{n} = \boldsymbol{e}_x\otimes\nabla(\cos\varphi\cos\psi) + \boldsymbol{e}_y\otimes(\cos\varphi\sin\psi) + \boldsymbol{e}_z\otimes\nabla(\sin\varphi), \tag{5.22}$$

where, since both φ and ψ are functions of bipolar coordinates (ξ,η), the gradients on the right-hand side must be computed as in Eq. (A7). Heeding that $d\ell/d\xi=1/H$, also by Eqs. (A3) and (A4), we finally express Eq. (5.20) as

$$F = -\frac{\kappa}{c}\int_0^{2\pi}\left\{\frac{1}{2}(1-\cosh\eta_{\mathrm{i}}\cos\xi)[\varphi_{,\xi}^2 - \varphi_{,\eta}^2 + \cos^2\varphi(\psi_{,\xi}^2 - \psi_{,\eta}^2)] + \sinh\eta_{\mathrm{i}}\sin\xi(\varphi_{,\xi}\varphi_{,\eta} + \cos^2\varphi\psi_{,\xi}\psi_{,\eta})\right\}d\xi, \tag{5.23}$$

where all functions in the integrand are computed at $\eta=\eta_{\mathrm{i}}$. This formula was employed to calculate numerically F.

In the special case $\varphi\equiv 0$ and $\psi\equiv-\vartheta_0$, use of Eq. (4.8) leads us to

$$F = \frac{\kappa\pi}{c}. \tag{5.24}$$

By Eq. (2.11), we can express Eq. (5.24) in terms of the scaled distance $\chi=h/r_{\mathrm{i}}$ between the cylinders:

$$F = \frac{2\kappa\pi(\varrho-\chi-1)}{r_{\mathrm{i}}\sqrt{[2\chi+\chi^2]\{[2\varrho-(\chi+1)]^2-1\}}}. \tag{5.25}$$

In the limit where $\chi\ll 1$, the leading term in h in Eq. (5.25) is

$$F = \frac{\pi\kappa}{\sqrt{r_{\mathrm{i}}}\sqrt{2h}}\sqrt{\frac{\varrho-1}{\varrho}}. \tag{5.26}$$

In particular, when $\varrho\to+\infty$, and so the outer cylinder approaches a flat wall, F diverges as $1/\sqrt{h}$, in accordance with the conclusions of Sonnet and Gruhn in [11], where a flat wall replaced the outer cylinder.

C. Torque

In the one-constant approximation, Ericksen's stress tensor is symmetric [see Eq. (5.19)]. Thus by the divergence

theorem, the integral in Eq. (5.5) vanishes whenever $\mathcal{S}$ is a closed surface. Here the total torque $\boldsymbol{M}$ then results only from the surface couples. It follows from Eq. (5.17) that the nontrivial component of $\boldsymbol{M}$ per unit height of the inner cylinder is given by

$$M = \int_{\mathcal{C}} \boldsymbol{e}_y \cdot \mathbf{L}\boldsymbol{\nu} d\ell. \tag{5.27}$$

Since in the one-constant approximation

$$\frac{\partial W}{\partial \nabla \boldsymbol{n}} = \kappa \nabla \boldsymbol{n},$$

Eq. (5.4) becomes

$$\mathbf{L}\boldsymbol{\nu} = \kappa \boldsymbol{n} \times (\nabla \boldsymbol{n})\boldsymbol{\nu}.$$

The outer unit normal $\boldsymbol{\nu}$ to the lateral surface of the inner cylinder is $\boldsymbol{\nu}=-\boldsymbol{e}_\eta$. With the aid of both Eqs. (5.21) and (5.22) we arrive at

$$M = -\kappa \int_0^{2\pi} (\cos\psi\varphi_{,\eta} + \sin\varphi\cos\varphi\sin\psi\psi_{,\eta}) d\xi, \tag{5.28}$$

where again the integrand is computed at $\eta=\eta_i$.

D. Numerical results

Forces and torques must be computed on stable equilibrium solutions. We saw in Sec. III that the planar solution $\boldsymbol{n}_0 \equiv \boldsymbol{e}_\eta$ is stable only when the dimensionless parameters (ϱ, δ) are chosen within the region S in Fig. 2. In particular, if the ratio $\varrho=r_o/r_i$ exceeds the critical value $\varrho^* \approx 8.46$, the planar solution loses its stability whenever the cylinders are drawn sufficiently close to one another, that is, whenever the dimensionless distance $\chi=h/r_i$ between them becomes small enough. Alternatively, for given χ, the point (ϱ, δ) falls within the unstable region U whenever ϱ is sufficiently large. Both these ways of crossing the border between S and U are explored below: F and M, as given by Eqs. (5.23) and (5.28), respectively, are computed in U on the escaped solution.

To appreciate the structural changes that the escaped solution undergoes upon varying the parameters ϱ and δ we also record the maximum value φ_{max} attained by the tilt angle φ across the region $\mathbb{B}$ as well as the spatial averages $\langle|\vartheta|\rangle$ and $\langle\varphi\rangle$ defined as

$$\langle|\vartheta|\rangle := \frac{\int_{\eta_o}^{\eta_i} d\eta \int_0^{2\pi} d\xi \frac{1}{H^2} |\vartheta(\xi,\eta)|}{A(\mathbb{B})}$$

$$\langle\varphi\rangle := \frac{\int_{\eta_o}^{\eta_i} d\eta \int_0^{2\pi} d\xi \frac{1}{H^2} \varphi(\xi,\eta)}{A(\mathbb{B})}, \tag{5.29}$$

where $A(\mathbb{B})=\int_{\eta_o}^{\eta_i} d\eta \int_0^{2\pi} d\xi \frac{1}{H^2}$ is the area of $\mathbb{B}$, and $1/H^2$ is the Jacobian $|J|$ of bipolar coordinates.

Figure 7 shows both F and M computed for $\chi=10$ as functions of $\varrho \geqslant 15$. For $15 \leqslant \varrho \leqslant 20.6$, the point (ϱ, δ) falls within the stability domain S for the planar solution, and so F is computed according to Eq. (5.25), while, in accordance with Eq. (5.28), M vanishes identically. For $\varrho > 20.6$, we computed F on both the planar and the escaped solutions: the corresponding graphs are represented by dashed and solid lines, respectively. The graph of M in Fig. 7(c) corresponds to the escaped solution, as $M \equiv 0$ for the planar solution. On the escaped solution, F is a monotonically decreasing function of ϱ, whereas M is monotonically increasing. The angle φ_{max} and the averages in Eq. (5.29) all increase with ϱ and saturate to a plateau; in particular, φ_{max} approaches 90° as $\varrho \to \infty$. Figure 8 shows similar graphs for $\chi=15$. The only qualitative difference with the graphs in Fig. 7 is in the behavior of F, which here fails to be monotonically decreasing in ϱ on the escaped solution: it attains its maximum at a value of ϱ close to, but different from the bifurcation point.

Ideally, keeping χ fixed and varying ϱ, we imagine to hold the inner cylinder fixed, while enclosing it within a cylinder of increasing radius kept at the same distance. This eventually destabilizes the planar solution. A different way to do this is by keeping δ fixed while increasing ϱ. In such a way, the distance between the cylinders' axes is kept fixed, while both the radius of the outer cylinder and the separation between the two cylinders are increased. By Eq. (2.12), in the limit as $\varrho \to \infty$ the outer cylinder is almost flat, while the inner cylinder is at the greatest distance from it. In Fig. 9, F and M are shown as functions of ϱ, for $\delta=5$. F is monotonically decreasing in ϱ on both planar and escaped solutions and tends to zero when $\varrho \to \infty$. M first increases and then decreases asymptotically to zero as $\varrho \to \infty$. The vanishing of both F and M as $\varrho \to \infty$ does not surprise us, since in this limit the distance between the two cylinders diverges. Clearly, we cannot expect appreciable mechanical actions on the inner cylinder in this case.

So far ϱ was varied, while either χ or δ was kept fixed. Thus we studied the effect of curvature on both the force and the torque transmitted by the liquid crystal in its stable equilibrium configuration. To study the effects of the distance between the cylinders, we now fix ϱ and explore the behavior of F and M when χ is varied. The bilogarithmic plot in Fig. 10 shows the behavior of F as a function of χ for $\varrho=20$ on both the planar and the escaped solutions. Here, by Eq. (2.12) χ ranges in the interval [0, 19], and the planar solution is stable for $\chi > 9.2$. For $\chi < 9.2$, the forces on the escaped and the planar solutions do not differ much: they tend to coalesce for $\chi \ll 1$.

We assume that in the limit as $\chi \to 0$ F obeys the power law $F=\chi^\gamma$, where the *limiting* exponent γ is given by [10]

$$\gamma := \lim_{\chi \to 0} \frac{\chi}{F} \frac{dF}{d\chi}. \tag{5.30}$$

It follows from Eq. (5.26) that the limiting exponent, if computed on the planar solution is $\gamma_p=\frac{1}{2}$. We evaluated the limiting exponent γ_e on the escaped solution for several values of ϱ. The difference $\gamma_e-\gamma_p$ is plotted in Fig. 11: though it increases when ϱ becomes larger, it never exceeds 0.03. For

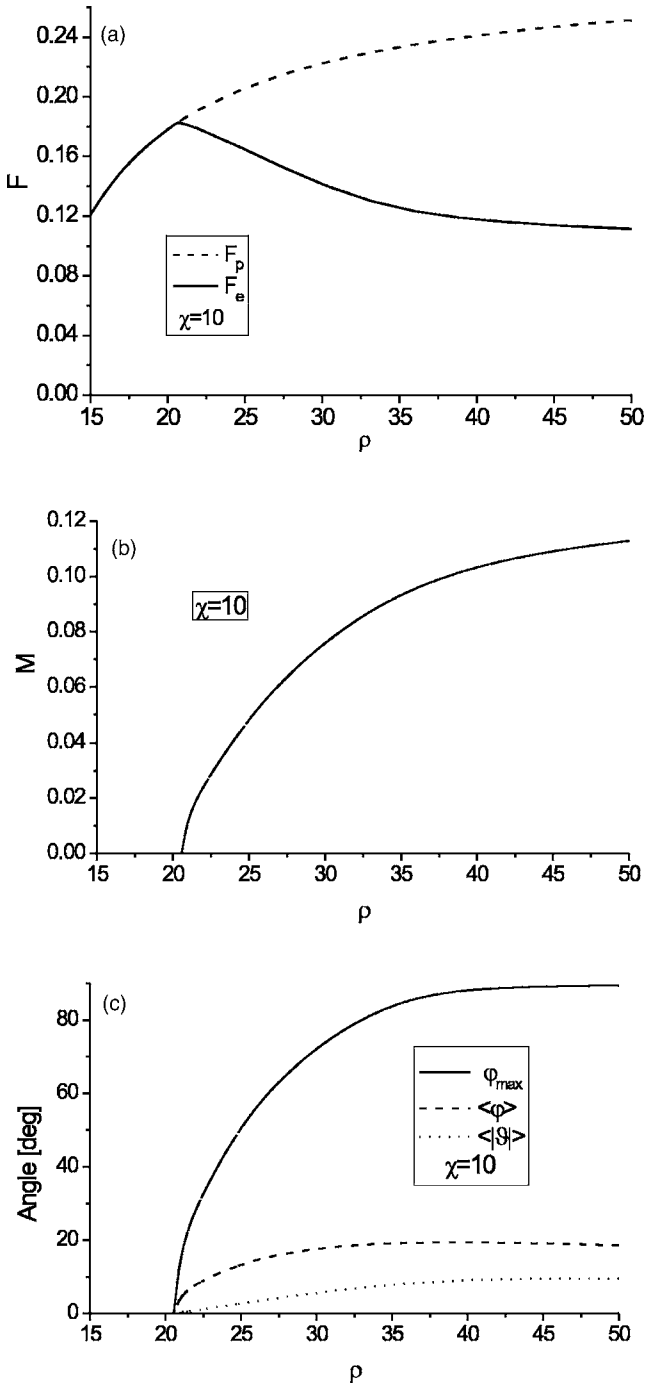

FIG. 7. (a) Plot of the elastic force F computed on the locally stable equilibrium configuration (solid line). It only lacks monotonicity at the point where the escaped solution bifurcates from the planar one. The dashed line represents the force F_p transmitted by the planar solution when it ceases to be locally stable. (b) Plot of the elastic torque M transmitted by the escaped solution. (c) Plots against ϱ of the maximum value φ_{max} of the tilt angle φ together with the spatial averages $\langle\varphi\rangle$ and $\langle|\vartheta|\rangle$ defined according to Eq. (5.29). When ϱ increases, all these quantities approach asymptotic values. All these graphs have been obtained at a fixed value $\chi=10$ of the dimensionless distance $\chi=h/r_i$ between the cylinders. Here and in the following figures, F is scaled to κ/r_i, while M is scaled to κ.

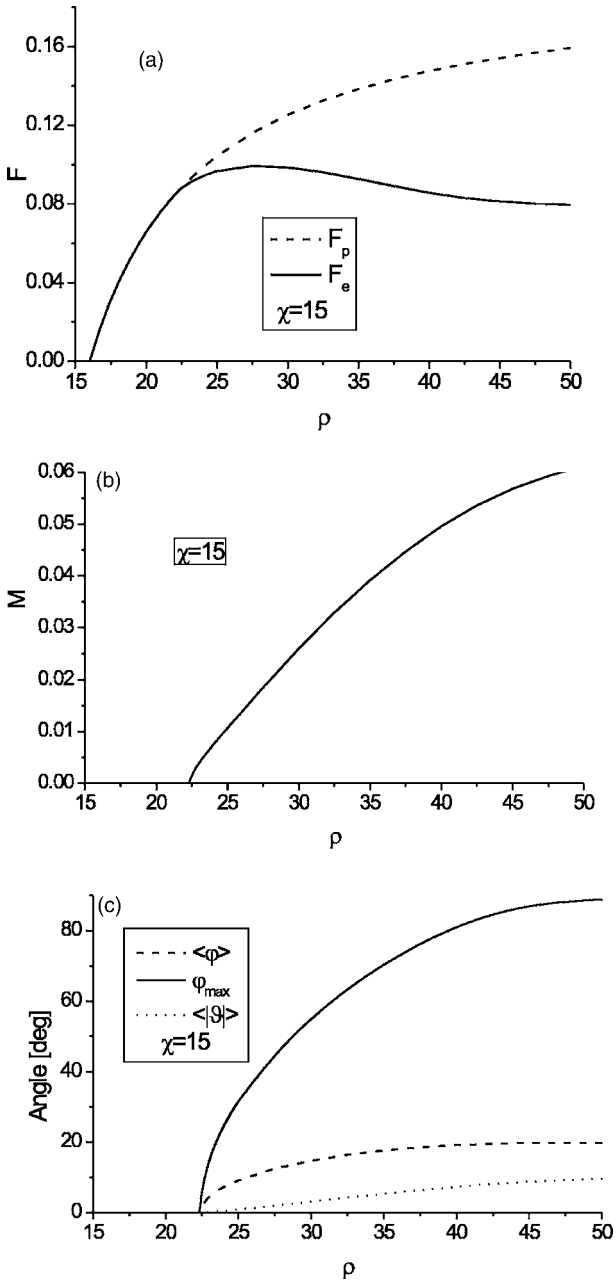

FIG. 8. This figure contains the plots of the same quantities as in Fig. 7, but for $\chi=15$. Two changes are worth noting in comparing these graphs with those in Fig. 7. First, increasing χ for a given ϱ decreases the value of all quantities F, M, φ_{max}, $\langle\varphi\rangle$, and $\langle|\vartheta|\rangle$. Second, there is a critical value of ϱ, different from the bifurcation point, at which the elastic force F transmitted by the escaped solution attains its maximum.

$\varrho > \varrho^* \approx 8.46$, the planar solution is unstable, but its limiting exponent is very close to the limiting exponent computed numerically on the stable escaped solution.

VI. CONCLUSIONS

We studied within the elastic director theory the equilibrium problem for a nematic liquid crystal confined within

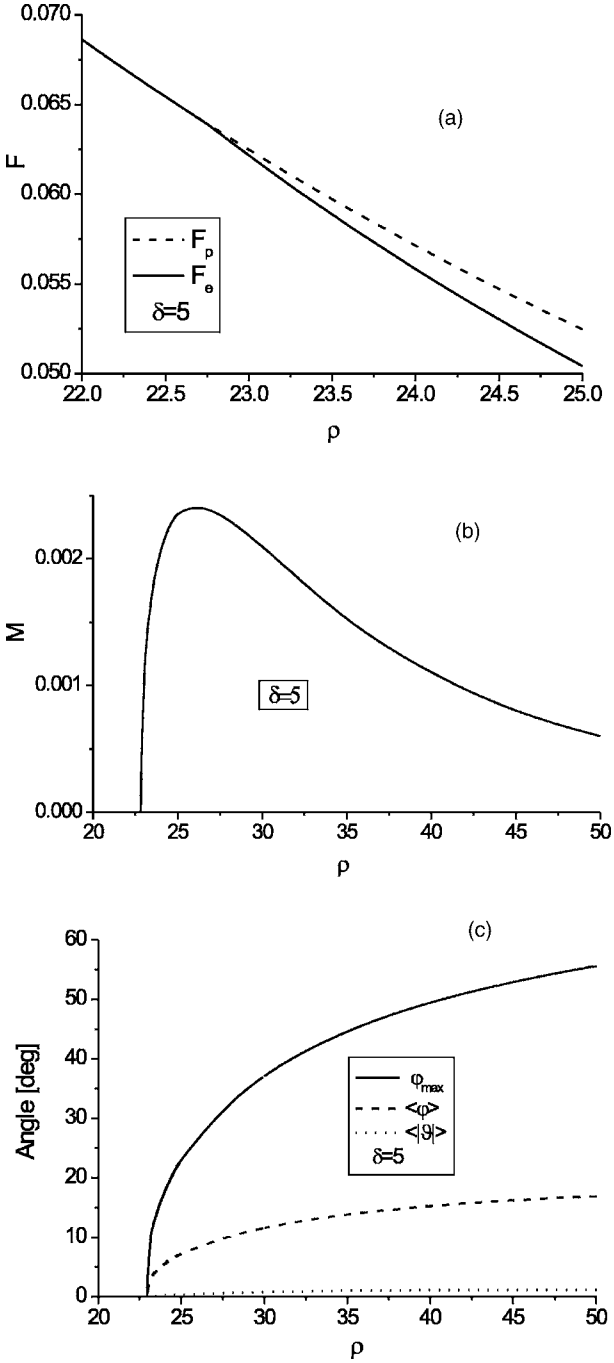

FIG. 9. Plots of the same quantities as in Figs. 7 and 8, but for $\delta=5$. The force F is a decreasing function of ϱ on both the planar and the escaped solution that approaches zero when $\varrho\to\infty$. The torque transmitted by the escaped solution is rather small and attains its maximum for ϱ close to the bifurcation point. The structural parameters $\varphi_{\max}$, $\langle\varphi\rangle$, and $\langle|\vartheta|\rangle$ are much smaller than their counterparts in Figs. 7 and 8 at a given ϱ.

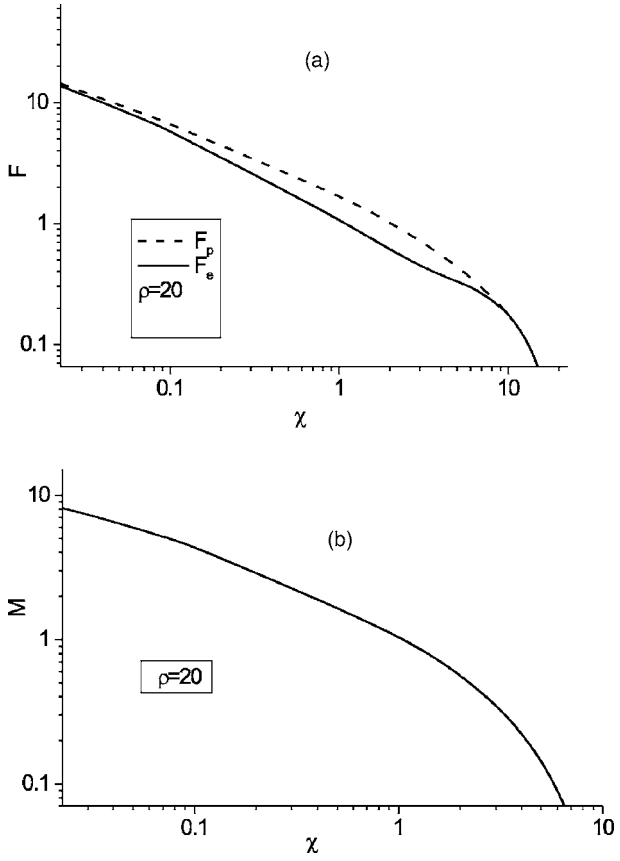

FIG. 10. (a) Bilogarithm plots of the force F computed on the escaped (F_e) and planar (F_p) solutions as a function of the dimensionless distance $\chi=h/r_i$ between the cylinders for $\varrho=r_o/r_i=20$. Here $0\leqslant\chi\leqslant 19$; the stability domain for the planar solution is crossed at $\chi=9.2$. F_e and F_p show a similar behavior as $\chi\to 0^+$. (b) Bilogarithm plot of the torque M, computed on the escaped solution, as a function of χ.

two parallel eccentric cylinders enforcing homeotropic anchoring on the lateral boundaries. The stability analysis revealed that the planar equilibrium configuration is unstable when either the radius of the outer cylinder is sufficiently larger than the radius of the inner cylinder or the distance between the cylinders is sufficiently small. In particular, when the outer cylinder degenerates into a flat wall, the planar solution is unstable for all separations between the wall and the remaining cylinder. When the planar solution loses its stability an escaped solution takes its place: the director

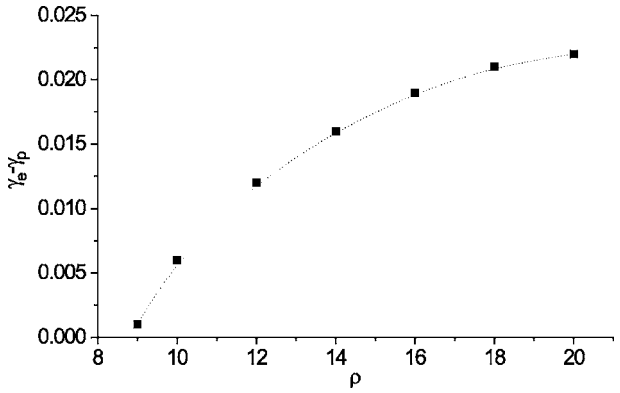

FIG. 11. Difference $\gamma_e-\gamma_p$ between the limiting exponent γ_e of the force F computed as in Eq. (5.30) for the escaped solution and the limiting exponent $\gamma_p=\frac{1}{2}$ determined analytically from Eq. (5.26) for the planar solution. The squares correspond to the values of ϱ for which γ_e was actually computed.

not only flips out of the plane orthogonal to the cylinders' axes, but its projection onto this plane also wobbles about the field lines of the planar equilibrium configuration. On this structure, the mechanical actions that the liquid crystal transmits from one cylinder to the other were also computed: both the force and the torque transmitted by the escaped solution were found to be monotonic functions of the distance h between the cylinders. When h is very small, the force diverges with a power law that only slightly differs from the $1/\sqrt{h}$ behavior predicted by Sonnet and Grühn [11], though their analysis strictly applies only to the planar solution, which we found unstable when the outer radius is sufficiently large.

The results of this paper are to be contrasted with those obtained by McKay and Virga [10], who studied within the order-tensor theory the equilibrium problem for a cylinder and a flat wall. They computed mechanical actions that were not monotonic functions of the distance between cylinder and wall. They interpreted such a lack of monotonicity as the onset of a snapping instability bringing the liquid crystal from the escaped structure into the planar structure in an ideal force—or torque—controlled experiment. The structural change accompanying this transition is signaled by a certain degree of biaxiality that arises in the vicinity of the cylinder in response to its curvature. Within the director theory these changes cannot be appreciated, and so they might indeed be real, thus justifying a nonmonotonic order force as opposed to a monotonic elastic force.

Whether this is the right way to reconcile the findings of this paper with [10] is not clear. A major obstacle still lies in the class of order tensors employed in [10]. These had everywhere $\boldsymbol{e}_\eta$ as an eigenvector, which in the uniaxial limit amounts to say that the director $\boldsymbol{n}$ is either parallel to $\boldsymbol{e}_\eta$ or orthogonal to it. This dichotomy is not confirmed by our analysis, which showed how in the escaped solution $\boldsymbol{n}$ can have nonvanishing components along all vectors of the movable frame $(\boldsymbol{e}_\xi, \boldsymbol{e}_\eta, \boldsymbol{e}_z)$. Thus the class of order tensors employed in [10] proves to be too narrow to encompass all the director equilibrium solutions found here, while it is large enough to describe the effects of biaxial order on the elastic force and torque. It remains to be seen whether these two studies can be reconciled within a general unconstrained class of order tensors.

ACKNOWLEDGMENTS

S. Kralj acknowledges the support of the COSLAB European Science Foundation program.

APPENDIX A: BIPOLAR CYLINDRIC COORDINATES

Much in the spirit of Appendix A of [15], we collect in this Appendix some mathematical properties of cylindric bipolar coordinates, which have been extensively used in this paper. In general, for a set of orthogonal curvilinear coordinates (q_1, q_2, q_3), the *metrical coefficients* (h_1, h_2, h_3) are defined as

$$h_k := \frac{1}{|\partial \boldsymbol{x}/\partial q_k|},$$

where $\boldsymbol{x}$ is the position vector of a point in the Euclidean space. For cylindric bipolar coordinates,

$$q_1 = \xi, \quad q_2 = \eta, \quad q_3 = z, \tag{A1}$$

and so we have

$$h_1 = h_2 = H := \frac{1}{c}(\cosh \eta - \cos \xi), \quad h_3 = 1. \tag{A2}$$

The unit tangent vector $\boldsymbol{e}_k$ to the coordinate curve q_i=const, q_j=const $(i \neq j \neq k)$ is given by

$$\boldsymbol{e}_k := h_k \frac{\partial \boldsymbol{x}}{\partial q_k},$$

where repeated indices are not summed. It follows from Eqs. (2.4) and (A1) that

$$\boldsymbol{e}_\xi = -\left[\frac{\sinh \eta \sin \xi}{\cosh \eta - \cos \xi}\boldsymbol{e}_x + \frac{1 - \cosh \eta \cos \xi}{\cosh \eta - \cos \xi}\boldsymbol{e}_y\right], \tag{A3}$$

$$\boldsymbol{e}_\eta = \left[\frac{1 - \cosh \eta \cos \xi}{\cosh \eta - \cos \xi}\boldsymbol{e}_x - \frac{\sinh \eta \sin \xi}{\cosh \eta - \cos \xi}\boldsymbol{e}_y\right], \tag{A4}$$

from which one obtains

$$\nabla \boldsymbol{e}_\xi = \frac{1}{c}[\sinh \eta \boldsymbol{e}_\eta \otimes \boldsymbol{e}_\xi - \sin \xi \boldsymbol{e}_\eta \otimes \boldsymbol{e}_\eta] \tag{A5}$$

and

$$\nabla \boldsymbol{e}_\eta = \frac{1}{c}[-\sinh \eta \boldsymbol{e}_\xi \otimes \boldsymbol{e}_\xi + \sin \xi \boldsymbol{e}_\xi \otimes \boldsymbol{e}_\eta]. \tag{A6}$$

Moreover, the gradient $\nabla\alpha$ and the Laplacian $\Delta\alpha$ of a smooth scalar field α in cylindric bipolar coordinates are expressed as

$$\nabla\alpha = H\left(\frac{\partial\alpha}{\partial\xi}\boldsymbol{e}_\xi + \frac{\partial\alpha}{\partial\eta}\boldsymbol{e}_\eta\right) + \frac{\partial\alpha}{\partial z}\boldsymbol{e}_z, \tag{A7}$$

$$\Delta\alpha = H^2\left(\frac{\partial^2\alpha}{\partial\xi^2} + \frac{\partial^2\alpha}{\partial\eta^2}\right) + \frac{\partial^2\alpha}{\partial z^2}. \tag{A8}$$

Equation (A7) can also be rewritten as

$$\nabla\alpha = \nabla_\parallel\alpha + \frac{\partial\alpha}{\partial z}\boldsymbol{e}_z,$$

where

$$\nabla_\parallel\alpha := H\left(\frac{\partial\alpha}{\partial\xi}\boldsymbol{e}_\xi + \frac{\partial\alpha}{\partial\eta}\boldsymbol{e}_\eta\right) \tag{A9}$$

is the *planar* gradient of α. In particular, it follows from Eq. (A8) that $\Delta\xi = \Delta\eta = \Delta z = 0$.

Similarly, for a vector field

$$\boldsymbol{u} = u_\xi \boldsymbol{e}_\xi + u_\eta \boldsymbol{e}_\eta + u_z \boldsymbol{e}_z$$

with components (u_ξ, u_η, u_z) smooth scalar functions of (ξ, η, z),

$$\nabla\boldsymbol{u} = u_\xi \nabla \boldsymbol{e}_\xi + \boldsymbol{e}_\xi \otimes \nabla u_\xi + u_\eta \nabla \boldsymbol{e}_\eta + \boldsymbol{e}_\eta \otimes \nabla u_\eta + \boldsymbol{e}_z \otimes \nabla u_z \tag{A10}$$

and

$$\Delta \boldsymbol{u} = \left[\Delta u_\xi - \frac{u_\xi}{H}\Delta H + 2H\left(\frac{\partial H}{\partial \xi}\frac{\partial u_\eta}{\partial \eta} - \frac{\partial H}{\partial \eta}\frac{\partial u_\eta}{\partial \xi} \right) \right] \boldsymbol{e}_\xi + \left[\Delta u_\eta - \frac{u_\eta}{H}\Delta H + 2H\left(\frac{\partial H}{\partial \eta}\frac{\partial u_\xi}{\partial \xi} - \frac{\partial H}{\partial \xi}\frac{\partial u_\xi}{\partial \eta} \right) \right] \boldsymbol{e}_\eta + \Delta u_z \boldsymbol{e}_z, \quad \text{(A11)}$$

where

$$\frac{\Delta H}{H} = \frac{1}{c^2}(\cosh^2 \eta - \cos^2 \xi). \quad \text{(A12)}$$

By Eq. (A9), Eq. (A11) can also be given the following form:

$$\Delta \boldsymbol{u} = \left[\Delta u_\xi - \frac{u_\xi}{H}\Delta H - \frac{2}{H}(\boldsymbol{\nabla}_\parallel u_\eta \times \boldsymbol{\nabla} H)\cdot \boldsymbol{e}_z \right] \boldsymbol{e}_\xi + \left[\Delta u_\eta - \frac{u_\eta}{H}\Delta H + \frac{2}{H}(\boldsymbol{\nabla}_\parallel u_\xi \times \boldsymbol{\nabla} H)\cdot \boldsymbol{e}_z \right] \boldsymbol{e}_\eta + \Delta u_z \boldsymbol{e}_z. \quad \text{(A13)}$$

For $\boldsymbol{u}=\boldsymbol{e}_\eta$, Eqs. (A13) and (A12) yield Eq. (2.13).

To ease the comparison between the different definitions of cylindric bipolar coordinates employed here and in [10], we heed that x and y are interchanged in the two papers and that the triple (ξ,η,c) introduced here corresponds to the triple $(\pi-u,v,a)$ of [10].

APPENDIX B: NUMERICAL METHODS

We used the over-relaxation method [16] to solve the Euler equations (4.5) and to perform the stability analysis of the planar configuration through Eqs. (3.7) and (3.8). Bipolar cylindric coordinates were discretized according to the stipulations $\xi_j=(j-1)\Delta\xi$, $\eta_k=(k-1)\Delta\eta+\eta_i$, $\Delta\xi=\frac{2\pi}{N_\xi-1}$, $\Delta\eta=\frac{\eta_o-\eta_i}{N_\eta-1}$, where j and k are integers ($j\in[1,N_\xi]$, $k\in[1,N_\eta]$), and $\eta_o=\eta_{N_\eta}$, $\eta_i=\eta_1$. We systematically chose $N_\eta=N_\xi=100$. We further expressed the discretized derivatives of a function $\alpha(\xi,\eta)$ at a point (ξ_j,η_k) in the usual way. Periodic boundary conditions were imposed at $\xi=0$ and $\xi=2\pi$ while strong boundary conditions at the cylinders' walls are enforced by setting $\alpha_{j,1}=\alpha_{j,N_\eta}=0$, where $\alpha_{j,k}:=\alpha(\xi_j,\eta_k)$ and α was either ϑ or φ.

The set of difference equations for $\alpha_{j,k}$ was solved by an iteration procedure that was stopped whenever the difference between the new and old value of $\alpha_{j,k}$ was less than $\varepsilon=10^{-8}$. We imposed this stringent criterion to determine accurately the transitional details at the second order transition. Increasing the number of grid points and decreasing ε did not affect the results to within the desired accuracy (0.1%). The robustness of the method against the choice of the initial guess function α was checked so that most computations have been performed by taking at the beginning α constant within the capillary.

More exactly, to obtain the stability diagram shown in Fig. 2, we checked whether the perturbation $\boldsymbol{u}$ relaxes to $\boldsymbol{0}$ or moves away from it. This latter behavior could be detected after a few iterations and served to mark the transition line separating the stable set S from the unstable set U. An indirect confirmation of these results is obtained by solving the Euler equations (4.4), which give structural details of the escaped solution. The structural transition between the planar and escaped solutions was found to be continuous.

APPENDIX C: COAXIAL CYLINDERS

Here, we apply the stability criterion put forward in [13] to derive the result obtained by Bethuel *et al.* in [14] on the instability of the radial configuration of the director $\boldsymbol{n}_0\equiv\boldsymbol{e}_r$ within two coaxial cylinders parallel to $\boldsymbol{e}_z$. In cylindrical coordinates (r,ϑ,z) the region occupied by the liquid crystal is described by the inequalities

$$r_i \leqslant r \leqslant r_o, \quad 0 \leqslant \vartheta \leqslant 2\pi, \quad \text{and} \quad -a \leqslant z \leqslant a.$$

Strong anchoring is enforced at $r=r_i$ and $r=r_o$, whereas periodic boundary conditions are enforced on the fictitious boundaries at $z=\pm a$. The radial configuration $\boldsymbol{n}_0\equiv\boldsymbol{e}_r$ solves Eq. (2.2) with

$$\lambda = \frac{\kappa}{r^2}.$$

We consider perturbations $\boldsymbol{u}$ of $\boldsymbol{n}_0$ depending solely on r, that is, we set

$$\boldsymbol{u} = u_\vartheta(r)\boldsymbol{e}_\vartheta + u_z(r)\boldsymbol{e}_z.$$

Since this parametrization guarantees that the constraint (3.2) is obeyed, we can set $\nu=0$ in Eq. (3.1); this latter equation now reads as

$$\left(\Delta u_\vartheta - \frac{u_\vartheta}{r^2}\right)\boldsymbol{e}_\vartheta + \Delta u_z \boldsymbol{e}_z + \left(\mu + \frac{1}{r^2}\right)(u_\vartheta \boldsymbol{e}_\vartheta + u_z \boldsymbol{e}_z) = \boldsymbol{0}. \quad \text{(C1)}$$

Projecting this equation along the movable frame $(\boldsymbol{e}_r,\boldsymbol{e}_\vartheta,\boldsymbol{e}_z)$, we get

$$[ru'_\vartheta]' + \mu r u_\vartheta = 0, \quad \text{(C2)}$$

$$[ru'_z]' + r\left(\mu + \frac{1}{r^2}\right)u_z = 0, \quad \text{(C3)}$$

where a prime stands for differentiation with respect to r. Strong anchoring at the bounding cylinders requires that

$$u_\vartheta(r_i) = u_\vartheta(r_o) = 0 \quad \text{and} \quad u_z(r_i) = u_z(r_o) = 0.$$

Just the same strategy adopted in Sec. III to prove that $u_\xi \equiv 0$ shows here that unstable modes have $u_\vartheta \equiv 0$. Hence we limit attention to Eq. (C3) where we set $r:=e^x r_i$ obtaining

$$u'_z(x) + (1 + \mu e^{2x})u_z(x) = 0, \quad \text{(C4)}$$

where now a prime denotes differentiation with respect to x, whereas μ has been rescaled to r_i^2. Equation (C4) is subject to the boundary conditions

$$u_z(0) = u_z(x_0) = 0,$$

where $x_0=\ln \varrho$. It follows from the Sturm-Liouville theory

(see Chap. VII of [21]) that the eigenvalue associated with an eigenfunction u of Eq. (C4) is given by

$$\mu = \frac{\int_0^{x_0} [(u')^2 - u^2]dx}{\int_0^{x_0} u^2 e^{2x} dx}. \tag{C5}$$

Moreover, by Wirtinger's inequality (see p. 185 of [22]),

$$\int_0^{x_0} u'^2 dx \geqslant \left(\frac{\pi}{x_0}\right) \int_0^{x_0} u^2 dx \tag{C6}$$

for all u vanishing at the end points of the interval $[0, x_0]$. Combining Eqs. (C5) and (C6), we see that if $\pi > x_0$ then $\mu > 0$, and so there are neither unstable nor marginal modes for Eq. (C1). Thus the radial solution $\boldsymbol{n}_0$ is stable whenever $\varrho_0 < e^{\pi}$. For $x_0 = \pi$, a direct inspection of Eq. (C4) with $\mu = 0$ reveals the existence of a marginal mode. This proves that $\varrho = e^{\pi}$ marks the limit of stability for the planar solution in the case of coaxial cylinders [14].

[1] R. G. Horn, J. N. Israelachvili, and E. Perez, J. Phys. (France) (France) **42**, 39 (1981).

[2] F. Bisi and E. G. Virga, in *Modeling of Soft Matter*, edited by M.-C. T. Calderer and E. M. Terentjev (Springer, New York, 2005), pp. 111–132.

[3] N. Schopohl and T. J. Sluckin, Phys. Rev. Lett. **59**, 2582 (1987).

[4] P. Palffy-Muhoray, E. C. Gartland, and J. R. Kelly, Liq. Cryst. **16**, 713 (1994).

[5] F. Bisi, E. C. Gartland, R. Rosso, and E. G. Virga, Phys. Rev. E **68**, 021707 (2003).

[6] R. Barberi, F. Ciuchi, G. E. Durand, M. Iovane, D. Sikharulidze, A. M. Sonnet, and E. G. Virga, Eur. Phys. J. E **13**, 61 (2005).

[7] R. Barberi, F. Ciuchi, G. Lombardo, R. Bartolino, and G. E. Durand, Phys. Rev. Lett. **93**, 137801 (2004).

[8] F. Bisi, E. G. Virga, and G. E. Durand, Phys. Rev. E **70**, 042701 (2004).

[9] B. Zappone, Ph. Richetti, R. Barberi, R. Bartolino, and H. T. Nguyen, Phys. Rev. E **71**, 041703 (2005).

[10] G. McKay and E. G. Virga, Phys. Rev. E **71**, 041702 (2005).

[11] A. Sonnet and T. Gruhn, J. Phys.: Condens. Matter **11**, 8005 (1999).

[12] Here the term *escaped* is used as a poetic licence to indicate that the director field has a nonzero component along the capillary axis. We do not mean that the director is parallel to this axis somewhere inside the capillary, as in the classical Cladis-Kléman-Meyer solution illustrated, for example, in Ref. [20].

[13] R. Rosso, E. G. Virga, and S. Kralj, Phys. Rev. E **70**, 011710 (2004).

[14] F. Bethuel, H. Brezis, B. D. Coleman, and F. Hélein, Arch. Ration. Mech. Anal. **118**, 149 (1992).

[15] J. Happel and H. Brenner, *Low Reynolds Number Hydrodynamics with Special Applications to Particulate Media* (Prentice-Hall, Englewood Cliffs, NJ, 1965).

[16] W. H. Press, B. P. Flannery, S. A. Teukolsky, and W. T. Vetterling, *Numerical Recipies* (Cambridge University Press, Cambridge, 1986).

[17] B. Kawohl, *Rearrangements and Convexity of Level Sets in PDE* (Springer, Berlin, 1985).

[18] J. L. Ericksen, Arch. Ration. Mech. Anal. **9**, 371 (1962).

[19] F. M. Leslie, Arch. Ration. Mech. Anal. **28**, 265 (1968).

[20] E. G. Virga, *Variational Theories for Liquid Crystals* (Chapman & Hall, London, 1994).

[21] H. Weinberger, *A First Course in Partial Differential Equations with Complex Variables and Transform Methods* (Blaisdell, New York, 1965).

[22] G. H. Hardy, J. E. Littlewood, and G. Pólya, *Inequalities*, 2nd ed.. (Cambridge University Press, Cambridge, 1952).